

# Towards Realistic Time-Resolved Simulations of Quantum Devices

Joseph Weston<sup>1,2</sup> and Xavier Waintal<sup>1,2</sup>

<sup>1</sup>Univ. Grenoble Alpes, INAC-SPSMS, F-38000 Grenoble, France

<sup>2</sup>CEA, INAC-SPSMS, F-38000 Grenoble, France

(Dated: April 6, 2016)

We report on our recent efforts to perform realistic simulations of large quantum devices in the time domain. In contrast to d.c. transport where the calculations are explicitly performed at the Fermi level, the presence of time-dependent terms in the Hamiltonian makes the system inelastic so that it is necessary to explicitly enforce the Pauli principle in the simulations. We illustrate our approach with calculations for a flying qubit interferometer, a nanoelectronic device that is currently under experimental investigation. Our calculations illustrate the fact that many degrees of freedom (16,700 tight-binding sites in the scattering region) and long simulation times (80,000 times the inverse bandwidth of the tight-binding model) can be easily achieved on a local computer.

## I. INTRODUCTION

With the technical progress of low temperature (mK) and high frequency (GHz to THz) experimental setups, high frequency quantum transport experiments have recently moved from theory to the lab. In particular, coherent single electron sources with well defined release times<sup>1</sup> or energies<sup>2</sup> have been demonstrated; a key milestone for engineering non-trivial propagating quantum states. In parallel, quantum propagation itself has been observed along quantum Hall edge states<sup>3–5</sup> and at terahertz frequencies in carbon nanotubes<sup>6</sup>. Being able to perform computer simulations of these types of experiment is an important step needed for the development of the field.

Simulations of quantum transport in d.c. are now routinely performed. When going from d.c. to the time domain, an important difficulty emerges even in the non-interacting limit: the necessity to enforce the Pauli principle. Indeed, in presence of time-dependent terms in the Hamiltonian, the energy of an electron can change, possibly towards a state that is *already occupied*. As such processes are strictly forbidden, the many-body character of quantum transport, which can often be forgotten in d.c. transport, must be taken care of properly.

A standard route for doing so is the non-equilibrium Green's functions (NEGF) formalism, which has been around since the 90s<sup>7,8</sup>. A direct numerical integration of the NEGF equations is possible but rather cumbersome even for non-interacting systems (the focus of this paper). Another approach is the generalization of the Landauer-Büttiker scattering matrix formalism to the time domain<sup>9</sup>. A last approach is the partition-free approach<sup>10–12</sup>. These three approaches are strictly equivalent – at the mathematical level – for non interacting (or mean field) models<sup>13</sup>.

In our opinion, the most transparent and efficient way of dealing with the Pauli principle is to use the fact that the antisymmetric character of a many-body wave function is preserved by the quantum dynamics. To be specific, let us consider a *finite* system  $S$  initially at zero

temperature, described by the following Hamiltonian,

$$\hat{H}(t) = \sum_{i,j \in S} H_{ij}(t) \hat{c}_i^\dagger \hat{c}_j \quad (1)$$

where  $\hat{c}_i^\dagger$  ( $\hat{c}_j$ ) is a creation (destruction) operator for a one-particle state on site  $i$  ( $j$ ), and  $H_{ij}(t)$  are matrix elements of the Hamiltonian, which we will collectively refer to as the matrix  $\mathbf{H}(t)$ . The “sites”  $i$  may label spatial degrees of freedom as well as any internal degrees of freedom such as spin or orbitals. We suppose that the time-dependent perturbation starts at  $t > 0$ , so that for  $t \leq 0$  the system can be characterized by its eigenstates  $\phi_\alpha$

$$\mathbf{H}(t=0)\phi_\alpha = E_\alpha\phi_\alpha. \quad (2)$$

Introducing the operators  $\hat{d}_\alpha = \sum_i [\phi_\alpha]_i \hat{c}_i$ , ( $[\phi_\alpha]_i$  is the component of  $\phi_\alpha$  on site  $i$ ) the many-body state at  $t = 0$  is simply a Slater determinant of all the filled states at energies lower than the Fermi energy  $E_F$ :

$$|\Psi(t=0)\rangle = \prod_{E_\alpha < E_F} \hat{d}_\alpha^\dagger |0\rangle, \quad (3)$$

where daggers denote Hermitian conjugation and  $|0\rangle$  is the vacuum state. In the same way, the solution at finite time can be written as

$$|\Psi(t)\rangle = \prod_{E_\alpha < E_F} \hat{d}_\alpha^\dagger(t) |0\rangle \quad (4)$$

with

$$\hat{d}_\alpha(t) = \sum_i [\psi_\alpha(t)]_i \hat{c}_i, \quad (5)$$

where the one-body state  $\psi_\alpha(t)$  satisfies the Schrödinger equation,

$$i\hbar \frac{\partial}{\partial t} \psi_\alpha(t) = \mathbf{H}(t)\psi_\alpha(t) \quad (6)$$

and the initial condition

$$\psi_\alpha(t=0) = \phi_\alpha. \quad (7)$$

In other words, one only needs to evolve all the filled *one-body* states in time and use these to calculate observables. For instance the average number of particles on site  $i$  is simply given by,

$$\langle \hat{c}_i^\dagger(t) \hat{c}_i(t) \rangle = \sum_{E_\alpha < E_F} |\psi_\alpha(t)|_i^2 \quad (8)$$

The approach developed below (which can be found in Ref.<sup>13</sup> and Ref.<sup>14</sup>) follows essentially the above line of thought with 2 caveats: (i) one needs to extend the reasoning to infinite systems, i.e. systems connected to macroscopic electrodes. This implies that the filled states now form a continuum. (ii) The system at  $t = 0$  can be in an out-of-equilibrium state characterized by the different electrodes having different (electro-)chemical potentials and possibly different temperatures. Despite these difficulties we recently developed the “source-sink” algorithm<sup>14</sup> that scales linearly with the number of degrees of freedom in the scattering region *and* required simulation time. This algorithm has been applied recently to various cases including electronic interferometers<sup>15,16</sup>, quantum Hall effect<sup>17</sup>, normal-superconducting junctions<sup>18</sup>, Floquet topological insulators<sup>19</sup>, Josephson junction<sup>14</sup> and the calculation of the quantum noise of voltage pulses<sup>20</sup>. The favorable scaling properties are put to good use in the present article, where we treat systems with up to 16,700 degrees of freedom in the scattering region simulated up to times of 80,000 times the inverse bandwidth (the smallest time scale of the problem). The simulations take just over two hours using a few hundred CPU cores.

In the rest of this article, we will first review our numerical method with a fresh emphasis on the summation over filled states. In the final part, we will simulate an interesting “flying qubit” device which is currently the focus of an important experimental effort<sup>21–23</sup>.

## II. NUMERICAL METHOD

In this section we will succinctly describe the recently developed source-sink algorithm mentioned in the previous section. For brevity we shall leave a full derivation to previously published works<sup>13,14</sup>.

Let us now consider – in contrast to section I – an *open* quantum system without interactions consisting of a central scattering region  $S$  connected to semi-infinite periodic *leads*  $L$  such that the Hamiltonian can be written as

$$\hat{H}(t) = \sum_{i,j \in S} H_{ij}(t) \hat{c}_i^\dagger \hat{c}_j + \sum_{i,j \in L} H_{ij}(t) \hat{c}_i^\dagger \hat{c}_j + \sum_{i \in S, j \in L} H_{ij} \hat{c}_i^\dagger \hat{c}_j + h.c. \quad (9)$$

where  $H_{ij}(t)$  are now elements of an *infinite* matrix  $\mathbf{H}(t)$ . Note that even if the leads contain some uniform time-dependent voltage, the Hamiltonian can always be

brought into the form of eq. (9) by an appropriate gauge transformation. As in section I we shall make the restriction that the time-dependent perturbations start at  $t > 0$ , so that for  $t \leq 0$  the system can be characterized by its *scattering states*  $\psi_{\alpha E}^{st}$  labelled by their energy  $E$  and incoming channel  $\alpha$  in the leads:

$$\mathbf{H}(t=0) \psi_{\alpha E}^{st} = E \psi_{\alpha E}^{st}. \quad (10)$$

Using the periodic structure of the scattering states in the leads transforms eq. (10) into a linear system that can be solved using efficient techniques<sup>24,25</sup>; we use the Kwant<sup>26</sup> quantum transport package to obtain the  $\psi_{\alpha E}^{st}$ . Once we have the scattering states we can define the time-evolved scattering states using the time-dependent Schrödinger equation:

$$i \frac{\partial}{\partial t} \psi_{\alpha E}(t) = \mathbf{H}(t) \psi_{\alpha E}(t) \quad (11)$$

with the initial condition

$$\psi_{\alpha E}(0) = \psi_{\alpha E}^{st}. \quad (12)$$

As eq. (11) is defined on the full, *infinite* domain, it is not very useful for direct numerical simulation. In the source-sink algorithm, one replaces eq. (11) with a different – yet equivalent – problem in order to obtain the time-evolved scattering states in the central region. This consists of solving the following differential equation:

$$i \frac{\partial}{\partial t} \bar{\psi}_{\alpha E}(t) = [\mathbf{H}(t) - E] \bar{\psi}_{\alpha E}(t) + S(t) + \mathbf{\Sigma} \bar{\psi}_{\alpha E}(t) \quad (13)$$

where  $\psi_{\alpha E}(t) = [\bar{\psi}_{\alpha E}(t) - \psi_{\alpha E}^{st}] e^{-iEt}$ ,  $S(t) = \mathbf{H}(t) \psi_{\alpha E}^{st}$  is the source term, and  $\mathbf{\Sigma}$  – the sink – is a diagonal matrix that is 0 in the central region and takes complex values in a finite portion of the leads. Equation (13) is solved over the scattering region plus this finite portion of the leads, with the initial condition  $\bar{\psi}_{\alpha E}(0) = 0$ . Once we have the time-evolved scattering states we can calculate the thermal averages of physical quantities by integrating over the scattering states that were occupied at  $t = 0$ . The current between sites  $i$  and  $j$ , for example, can be written as

$$I_{ij}(t) = \sum_{\alpha} \int \frac{dE}{2\pi} f_{\alpha}(E) I_{\alpha;ij}(E, t), \quad (14)$$

where

$$I_{\alpha;ij}(E, t) = 2 \text{Im} \left( [\psi_{\alpha E}^\dagger(t)]_i H_{ij}(t) [\psi_{\alpha E}(t)]_j \right), \quad (15)$$

and  $f_{\alpha}(E)$  is the Fermi-Dirac distribution for the lead that contains mode  $\alpha$ . More generally the Retarded and Lesser Green’s functions ( $G_{ij}^R(t, t')$  and  $G_{ij}^<(t, t')$ ) can be computed using:

$$G_{ij}^<(t, t') = \sum_{\alpha} \int \frac{dE}{2\pi} f_{\alpha}(E) [\psi_{\alpha E}(t)]_i [\psi_{\alpha E}^\dagger(t')]_j \quad (16)$$

$$G_{ij}^R(t, t') = -i\Theta(t - t') \sum_{\alpha} \int \frac{dE}{2\pi} [\psi_{\alpha E}(t)]_i [\psi_{\alpha E}^\dagger(t')]_j \quad (17)$$

where  $\Theta(t - t')$  is the Heaviside function.

### A. Noise properties

We can even go beyond simple one-particle observables and look at two-particle observables such as current correlations and noise<sup>20</sup>. This is possible because the Hamiltonian is quadratic and we can therefore use Wick's theorem to express these observables as products of the single-particle Green's functions. Here we shall explicitly show the expressions for the current noise.

We define the current-current correlation function as

$$S_{\mu\nu}(t, t') = \left\langle \left( \hat{I}_\mu(t) - \langle \hat{I}_\mu(t) \rangle \right) \times \left( \hat{I}_\nu(t') - \langle \hat{I}_\nu(t') \rangle \right) \right\rangle, \quad (18)$$

with the operator for current flowing across an interface  $\mu$  defined as

$$\hat{I}_\mu(t) = \sum_{\langle i,j \rangle \in \mu} H_{ij}(t) c_i^\dagger(t) c_j(t) - H_{ji}(t) c_j^\dagger(t) c_i(t), \quad (19)$$

where the sum is performed over pairs of sites on opposite sides of the interface. Expressing this quantity in terms of the scattering states of the system, one arrives at

$$S_{\mu\nu}(t, t') = \sum_{\alpha, \beta} \int \frac{dE}{2\pi} \int \frac{dE'}{2\pi} f_\alpha(E) (1 - f_\beta(E')) \times I_{\mu, EE'}(t) [I_{\nu, EE'}(t')]^*, \quad (20)$$

where the quantity  $I_{\mu, EE'}(t)$  is closely related to the initial current operator

$$I_{\mu, EE'}(t) = \sum_{\langle i,j \rangle \in \mu} \left( [\psi_{\beta E'}^\dagger(t)]_i H_{ij}(t) [\psi_{\alpha E}(t)]_j - [\psi_{\beta E'}^\dagger(t)]_j H_{ji}(t) [\psi_{\alpha E}(t)]_i \right). \quad (21)$$

Equation (20) relates the typical output of a time-dependent simulation (right-hand side) to the noise properties (left-hand side). As an example, the total number of transmitted particles  $\hat{n}_\mu$  over a duration  $\Delta$ , defined as

$$\hat{n}_\mu = \int_{-\Delta/2}^{\Delta/2} dt \hat{I}_\mu(t), \quad (22)$$

can be calculated from the above expression and one arrives at a simple closed expression in terms of the time-dependent wave functions:

$$\text{var}(\hat{n}_\mu) = \sigma_{st}^2 \Delta + 2\sigma_{mix} + \bar{\sigma}^2 + O(1/\Delta) \quad (23)$$

with

$$\sigma_{st}^2 = \sum_{\alpha, \beta} \int \frac{dE}{2\pi} f_\alpha(E) (1 - f_\beta(E)) |I_{\mu, EE}(0)|^2 \quad (24)$$

$$\sigma_{mix} = \sum_{\alpha, \beta} \int \frac{dE}{2\pi} f_\alpha(E) (1 - f_\beta(E)) \text{Re}[\bar{N}_{EE}^* I_{\mu, EE}(0)] \quad (25)$$

$$\bar{\sigma}^2 = \sum_{\alpha, \beta} \int \frac{dE}{2\pi} \int \frac{dE'}{2\pi} f_\alpha(E) [1 - f_\beta(E')] |\bar{N}_{EE'}|^2 \quad (26)$$

with  $\bar{N}_{EE'}$  defined as

$$\bar{N}_{EE'} = \int_{-\infty}^{\infty} dt \left[ I_{\mu, EE'}(t) - I_{\mu, EE'}(0) e^{-i(E-E')t} \right]. \quad (27)$$

### B. Performing the Energy Integral

The above is a complete prescription for calculating the expectation value of time-resolved quantities in non-interacting nanoelectronics systems with semi-infinite leads. While eq. (13) can be solved numerically using standard techniques (we use a Runge-Kutta-Fehlberg adaptive scheme<sup>27</sup>), the energy integration needed to compute the thermal average can require a little more care. In particular, the integrands of expressions such as eq. (14) typically have (integrable) divergences at energies where the bands open. This is because the scattering states are normalized so that they carry unit current (so that the scattering matrix is unitary), which means that they diverge as  $1/\sqrt{v_\alpha(E)}$ , where  $v_\alpha(E) = dE_\alpha/dk$  is the group velocity of mode  $\alpha$  at energy  $E$ . For one-particle observables such as the current this means that the integrand diverges as  $1/v_\alpha(E)$  near the energy  $E_\alpha$  at which the mode  $\alpha$  opens (although as  $v_\alpha(E) \propto \sqrt{E}$  near the band edge, this divergence is integrable). This can be solved simply by choosing to integrate in momentum instead of energy; the  $dE/dk$  Jacobian factor cancels the divergence. When integrating in momentum one must make sure to only integrate over regions where  $v_\alpha(k) > 0$ , as these states are *incoming* into the system (i.e. they correspond to our scattering states). Equations (14) and (15) can thus be rewritten as

$$I_{ij}(t) = \sum_{\alpha} \int_{-\pi}^{\pi} \frac{dk}{2\pi} f_\alpha(k) \Theta[v_\alpha(k)] v_\alpha(k) I_\alpha(k, t), \quad (28)$$

and

$$I_\alpha(k, t) = 2 \text{Im} \left( [\psi_{\alpha k}^\dagger(t)]_i H_{ij}(t) [\psi_{\alpha k}(t)]_j \right). \quad (29)$$

Figure 1 shows the calculated  $I_\alpha(E, t)$  and  $v_\alpha(k)I(k, t)$  at  $t = 100$  (in units of the inverse bandwidth) for the mode coming from the left-hand lead in a perfect 1D chain after the application of a voltage pulse on the left-hand lead. We clearly see the  $1/v_\alpha(E)$  divergence in  $I_\alpha(E)$  at  $E = 0$  in fig. 1d, which is regularized by the change of variables to  $k$ , shown in fig. 1c.

Once the integration regions have been defined the integral is computed by using a Gauss-Kronrod 15(7) point embedded scheme<sup>28</sup>. Figure 2 compares the error scaling as a function of the number of integrand evaluations for this Gauss-Kronrod rule and Simpson's rule, applied to both the energy and k-space integrations, of the integrands shown in fig. 1. We clearly see that the k-space integral has significantly better scaling in this case due to the regularized singularity at the band edge. In addition, we see that the Gauss-Kronrod rule is capable

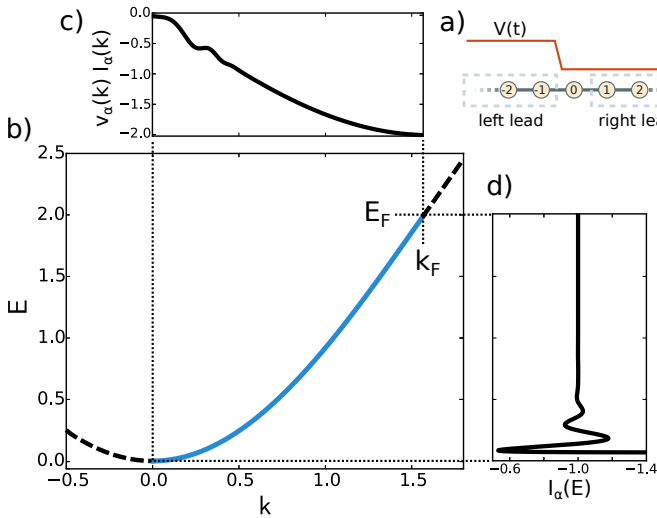


FIG. 1. An illustration of the difference between the energy and momentum integration techniques applied to a 1D chain with a gaussian voltage pulse applied. Times are given in units of the inverse bandwidth. a) Sketch of the simulated system. b) The band structure for the left lead. c) Integrand in  $k$ -space to calculate the current at  $t = 100$ . d) Integrand in energy to calculate the current at  $t = 100$ .

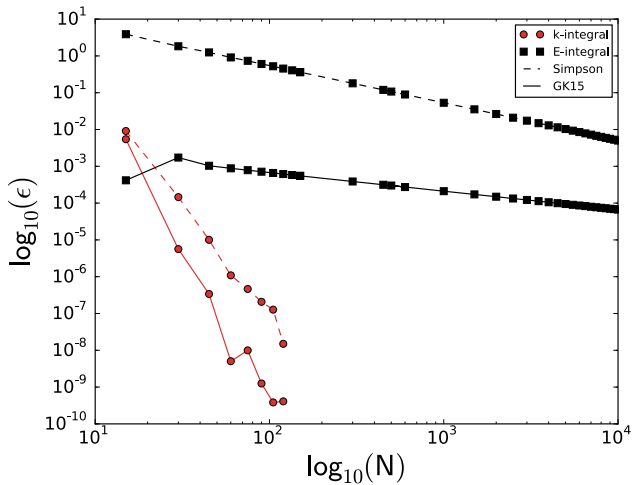


FIG. 2. Comparison of the error  $\epsilon$  for integration along  $k$  and energy using different integration methods – Simpson's rule and Gauss-Kronrod 15(7) (GK15) – as a function of the number of integrand evaluations,  $N$ . The error was calculated by subtracting the results of the integrals from a reference calculation performed using a  $k$ -space integration and the GK15 rule with 667 subregions (10005 integrand evaluations).

of achieving orders of magnitude greater accuracy for a given number of integrand evaluations. We note that we can benefit from this reduction only because our problem is formulated in the continuum, and so we are calculating *integrals* (as opposed to discrete sums) that can be evaluated numerically by discretizing in any way we please. If instead we had started from a (possibly large) finite

system, the choice of  $k$  points would have been dictated by the manner in which we truncated the infinite system.

An additional advantage of embedded rules such as Gauss-Kronrod is that they allow an error estimate to be calculated with no extra integrand evaluations. The integration region can then be bisected and the integral re-computed on the subregions if the error is found to be unacceptably high. Also, such schemes have the advantage that one does not need to evaluate the integrand on the boundary, as one does for schemes such as Simpson's rule. This is advantageous for our purposes as the scattering problem is ill-conditioned at energies where new bands open, so one needs to add an artificial offset to the integration boundaries when using a scheme that requires integrand evaluations on the boundary. The problem of using an adaptive scheme is that re-computing the integrand is computationally expensive (it corresponds to re-evolving wavefunctions from  $t = 0$  up to the time at which we wish to calculate the observable). For the specific case of systems that only have time-dependence in the voltage in the leads, we have found that a useful technique is to already subdivide the integration regions at  $t = 0$ , so as to obtain a good estimate for the observable at that time (when computing the integrand is computationally cheap; there is no time evolution to do!). At later times the integral is typically well-estimated by using this initially-chosen set of subintervals, and requires fewer additional subdivisions. In addition, any known structure of the problem (e.g. positions of resonances etc.) can also aid in an effective initial choice of subregions.

### III. APPLICATION TO A FLYING QUBIT INTERFEROMETER

We shall now apply the source-sink algorithm to a flying qubit interferometer in a split-wire setup. Such a setup has recently been realized experimentally<sup>21</sup> and was also studied numerically in d.c., however here we shall perform time-resolved simulations of a charge pulse injected into the interferometer by a voltage pulse applied to one of the contacts.

A sketch of the setup is shown in fig. 3. We shall treat the system as two quasi-1D wires that lie parallel to one another. The two wires are labelled  $\uparrow$  and  $\downarrow$  and can be interpreted as the two states of a (flying) qubit. They are (rather weakly) connected only in a finite region of length  $L$  (shown as the red region in fig. 3). A negatively polarized top-gate placed over the center of the wire in the coupling region allows the coupling between the wires to be tuned by altering the gate voltage,  $V_g$ . Under the gate ( $x \approx 0$ ), the potential falls from  $\infty$  to  $V_g$  adiabatically (to avoid spurious reflection), so that the effective length of the coupling region is  $\tilde{L}$ . In addition there is a back-gate at voltage  $V_b$  placed over the whole coupling region that allows us to control the potential there and hence the number of open conducting channels. This potential falls adiabatically to 0 before reaching the leads

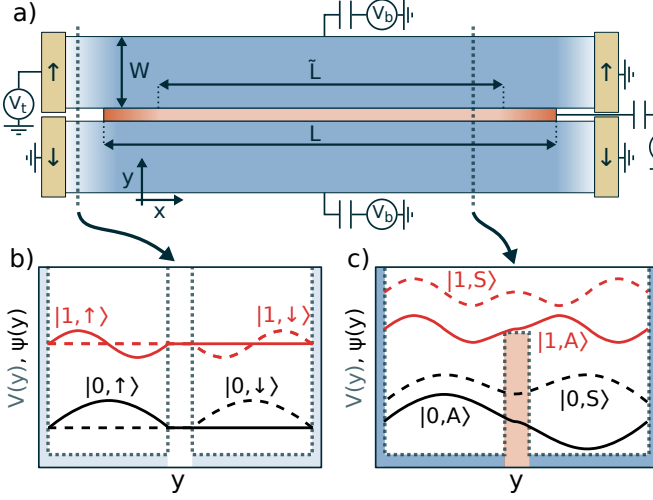


FIG. 3. a) Sketch of the split-wire system with the coupling region in red (controlled by gate voltage  $V_g$ ), a global backgate controlled by  $V_b$ , and 4 leads which are all grounded except for left lead  $\uparrow$ , which has a (time-dependent) bias voltage  $V_t$  applied.  $L$  measures the total coupling region length,  $\tilde{L}$  measures the effective coupling region length, and  $W$  measures the width of an individual wire. b) Sketch of the 4 lowest energy transverse modes before the coupled region, along with the transverse potential,  $V(y)$ . The states  $|n, \uparrow\rangle$  and  $|n, \downarrow\rangle$  are degenerate. c) Sketch of the 4 lowest energy transverse modes in the coupled region, along with the transverse potential,  $V(y)$ .

(shown as the blue color gradient in fig. 3). There is also a voltage source attached to lead  $\uparrow$  on the left that can apply a time-dependent bias  $V_t$  to the system. We treat the voltage drop as being abrupt at the interface between the lead  $\uparrow$  on the left and the central region. In order to simulate this model using the source-sink algorithm we first discretize it onto a square lattice of spacing  $a$  in order to obtain a tight-binding Hamiltonian of the form eq. (9).

### A. d.c. Characterization

We shall now look at d.c. transport in this system, in order to show that it can be thought of as an interferometer. This point of view will be invaluable when interpreting the time-resolved simulations in section III B. In order to calculate the d.c. conductance  $G_{\sigma'\sigma}$  between lead  $\sigma$  on the left and lead  $\sigma'$  on the right ( $\sigma \in \{\uparrow, \downarrow\}$ ) we need only use the Landauer formula<sup>29,30</sup>:

$$G_{\sigma'\sigma} = \frac{2e^2}{h} D_{\sigma'\sigma} \quad (30)$$

where  $D_{\sigma'\sigma}$  is the transmission from lead  $\sigma$  on the left to lead  $\sigma'$  on the right, defined by

$$D_{\sigma'\sigma} = \sum_{n,m} T_{m\sigma',n\sigma} \quad (31)$$

where  $T_{m\sigma',n\sigma}$  is the transmission *probability* from mode  $|n, \sigma\rangle$  on the left to mode  $|m, \sigma'\rangle$  on the right (these modes are sketched in fig. 3). In all that follows we shall assume that inter-band scattering is negligible, i.e.  $T_{m\sigma',n\sigma} = \delta_{mn} T_{n\sigma',n\sigma}$  where  $\delta_{mn}$  is the Kronecker delta. The calculation of the transmission probabilities for this system was very well explained in section III.B of ref. [21], so here we will provide just an intuitive picture of what is happening. The full wavefunction in the uncoupled region can be written  $\Psi_{n,\sigma}(x, y) = \langle y | n, \sigma \rangle e^{ik_{n,\sigma}x}$ , where  $\sigma \in \{\uparrow, \downarrow\}$ , and its energy is  $E = E_{n,\sigma} + (\hbar^2/2m^*)k_{n,\sigma}^2$ , where  $E_{n,\sigma}$  is the energy of the transverse mode  $|n, \sigma\rangle$ . As the states  $|n, \uparrow\rangle$  and  $|n, \downarrow\rangle$  are degenerate for a given  $n$ , we can also define symmetric and antisymmetric superpositions:

$$\begin{aligned} |n, \uparrow\rangle &= (1/\sqrt{2})[|n, S_u\rangle + |n, A_u\rangle] \\ |n, \downarrow\rangle &= (1/\sqrt{2})[|n, S_u\rangle - |n, A_u\rangle], \end{aligned} \quad (32)$$

where the  $u$  subscript reminds us that these are transverse modes in the *uncoupled* region. In the coupled region we also have symmetric and antisymmetric modes  $|n, S\rangle$  and  $|n, A\rangle$ , and we suppose that the transition from the uncoupled to the coupled region is adiabatic, such that  $|n, S_u\rangle$  evolves into  $|n, S\rangle$  and  $|n, A_u\rangle$  evolves into  $|n, A\rangle$  with no inter-mode scattering. While  $|n, A_u\rangle$  and  $|n, S_u\rangle$  are degenerate,  $|n, A\rangle$  and  $|n, S\rangle$  are not. This means that for a given energy the states will have different longitudinal wavevectors,  $k_{n,A}$  and  $k_{n,S}$ . If we were initially in a state  $|n, \uparrow\rangle$  this means that a length  $\tilde{L}$  after the wires are coupled we will be in a state:

$$|\psi_{n,\uparrow}\rangle = \frac{1}{\sqrt{2}} \left[ e^{ik_{n,A}\tilde{L}} |n, A\rangle + e^{ik_{n,S}\tilde{L}} |n, S\rangle \right]. \quad (33)$$

The wires are then adiabatically uncoupled (near the right-hand leads) and we can write:

$$\begin{aligned} |\psi_{n,\uparrow}\rangle &= \frac{1}{2} \left[ \left( e^{ik_{n,S}\tilde{L}} + e^{ik_{n,A}\tilde{L}} \right) |n, \uparrow\rangle + \right. \\ &\quad \left. \left( e^{ik_{n,S}\tilde{L}} - e^{ik_{n,A}\tilde{L}} \right) |n, \downarrow\rangle \right]. \end{aligned} \quad (34)$$

We immediately see that the difference in wavevectors will give rise to interference between the symmetric and antisymmetric components. We can thus write down the transmission *amplitudes* for arriving on the right in  $|n, \uparrow\rangle$  or  $|n, \downarrow\rangle$  given that we were injected on the left in  $|n, \uparrow\rangle$ :

$$\begin{aligned} t_{n\uparrow,n\uparrow} &= \exp \left( i \frac{k_{n,A} + k_{n,S}}{2} \tilde{L} \right) \cos \left( \frac{\Delta k_n}{2} \tilde{L} \right) \\ t_{n\downarrow,n\uparrow} &= i \exp \left( i \frac{k_{n,A} + k_{n,S}}{2} \tilde{L} \right) \sin \left( \frac{\Delta k_n}{2} \tilde{L} \right), \end{aligned} \quad (35)$$

where  $\Delta k_n = k_{n,A} - k_{n,S}$ . The transmission probabilities can be calculated from these amplitudes using  $T_{n\sigma',n\sigma} = |t_{n\sigma',n\sigma}|^2$ .

We performed tight binding simulations of the d.c. split wire system using the Kwant<sup>26</sup> package. Figure 4 shows

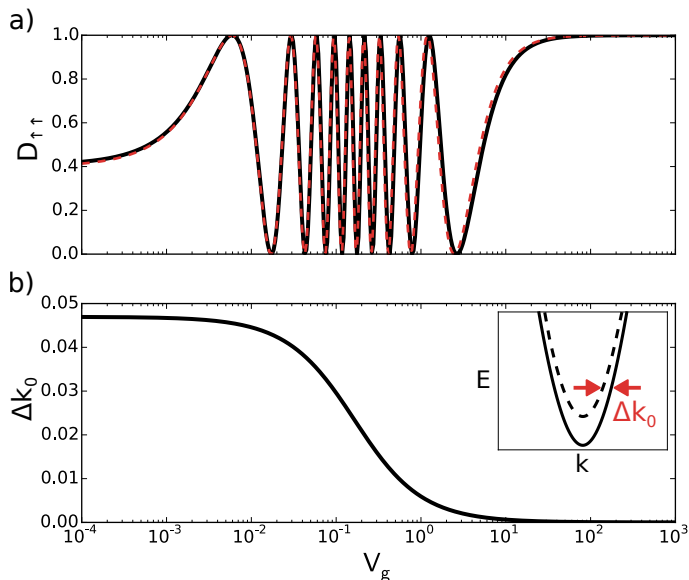


FIG. 4. d.c. simulation of split wire discretized with lattice parameter  $a = 2$  with  $L = 1400$ ,  $W = 20$ ,  $V_b = 0.11$  and  $E_F = 0.15$ . At this Fermi energy only the modes  $|0, \uparrow\rangle$  and  $|0, \downarrow\rangle$  in the coupled region are open. a) Black full line: transmission calculated from tight-binding simulation, red dashed line: transmission calculated using eq. (35) with  $\Delta k_0$  calculated from tight-binding and  $\tilde{L}$  as a fitting parameter. We used  $\tilde{L} = 1242$ . b) Tight-binding calculation of the difference in momentum between symmetric and antisymmetric modes in the coupling region. Both plots share the x-axis  $V_g$  scale.

how the wavevector difference changes as a function of the coupling gate voltage  $V_g$  and the effect that this has on the transmission  $D_{↑↑}$  from lead  $\uparrow$  on the left to lead  $\uparrow$  on the right. We clearly see regular oscillations when the wavevector difference changes linearly. As we go to very high gate voltages we effectively uncouple the two wires, which explains why  $D_{↑↑} \rightarrow 1$  in this limit. The red dashed line in fig. 4a shows  $D_{↑↑}$  calculated using eq. (35) where  $\Delta k_0$  has been calculated numerically from the tight binding model. We see a good fit of this simplified model with the full tight binding simulation.

Figure 5 shows the dispersion relations for the leads (subfigure a) and in the coupled region (subfigure b) calculated from the tight-binding model. We see in fig. 5c the transmission probabilities for being transmitted through the first and second modes from lead  $\uparrow$  on the left to lead  $\uparrow$  on the right. We see that the transmission probabilities are 0 before the corresponding modes in the central region open. Note that in order for  $T_{n\sigma', n\sigma}$  to be different from 0 we need *both* modes  $|n, A\rangle$  and  $|n, S\rangle$  to be open in the coupled region, as  $|n, \sigma\rangle$  is a linear combination of both. We see that the transmission probabilities oscillate as a function of energy. The reason for this is clear, as fig. 5b clearly shows that  $\Delta k_n$  changes as a function of energy. The inter-band transmission probabilities  $T_{m\sigma', n\sigma}$  (with  $m \neq n$ ) are not shown, but are 0 at all energies (validating the assumptions of the an-

alytical derivation above); this is because the transition from uncoupled to coupled region is done in an adiabatic manner.

One last point, which is perhaps a bit subtle, is that we expect to be able to see these interference effects even with a *large* number of open channels. Indeed, at the energy where the  $n + 1$  channel opens the  $\Delta k_{n+1}$  is much larger than the  $\Delta k_n$  at the same energy (see fig. 5b). This means that  $T_{n\sigma', n\sigma}$  oscillates much slower than  $T_{n+1\sigma', n+1\sigma}$  at the same energy, as can be clearly seen in fig. 5c. This separation in frequency of the different  $T_{n\sigma', n\sigma}$  means that the oscillations from the different channels will be clearly distinguishable in the full differential conductance  $G_{\sigma'\sigma}$ .

## B. Time-Dependent Simulations

Now we shall turn to time-resolved simulations of the split-wire. We apply a Gaussian voltage pulse to lead  $\uparrow$  on the left and measure the current  $I_{\uparrow}$  ( $I_{\downarrow}$ ) leaving the system on the right via lead  $\uparrow$  ( $\downarrow$ ). We also measure the injected current  $I_{in}$ . We place ourselves in a regime where only the modes  $|0, A\rangle$  and  $|0, S\rangle$  are open in the coupled region at the Fermi energy, and the pulse is not short/intense enough to excite higher energy modes. In d.c. this system has transmission  $D_{↑↑} = 0.1$  and  $D_{↓↑} = 0.9$ . Our system has  $L = 1400$  and  $W = 20$  with a discretisation parameter  $a = 2$ , and in total we have 16,700 sites in the scattering region.

Figure 6a shows the results of a simulation where the above-defined currents are measured. Due to the large characteristic length  $1/\Delta k_0$ , hence the large length of the system, we need to go to very long times (80,000 times the inverse bandwidth) in order to see the output current. The voltage pulse shown injects an average of  $\bar{n} = 2$  particles into system, where

$$e\bar{n} = \int_0^\infty dt I_{in}(t) \quad (36)$$

and  $e$  is the electronic charge. We clearly see that the output current oscillates between the  $\uparrow$  and  $\downarrow$  leads, which is counterintuitive; naïvely one would expect that the current in the two leads would have the same “shape” as a function of time, and that only the magnitudes would be different (proportional to the d.c. transmission).

Figure 6b shows the the number of particles transmitted on the right into lead  $\uparrow$  ( $n_{\uparrow}$ ) and  $\downarrow$  ( $n_{\downarrow}$ ) as a function of the number of injected particles. Rather than a simple proportionality relationship (where the slope would be given by the d.c. transmission), we see that the number of particles depends non-linearly on  $\bar{n}$  and even *oscillates* with  $\bar{n}$ . This curious behaviour can be understood by first understanding that prior to the voltage pulse, the Fermi sea is made of waves that form an effective two-path (Mach-Zehnder) interferometer. The effect of the voltage pulse is to twist the phase of these scattering



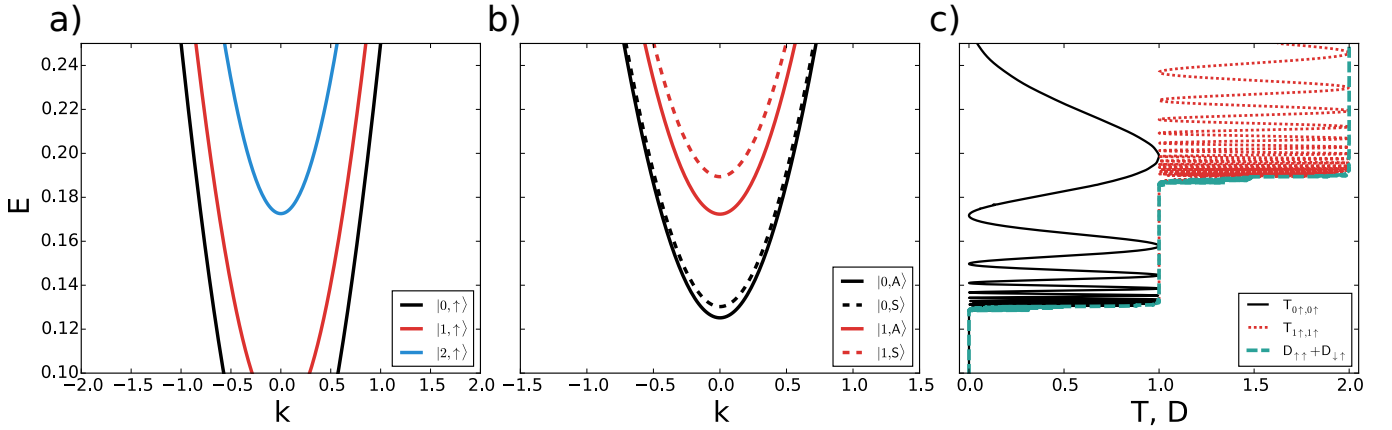


FIG. 5. Dispersion relations and transmissions for the split wire discretized with lattice parameter  $a = 2$  with  $L = 1400$ ,  $W = 20$ ,  $V_g = 0.27$  and  $V_b = 0.11$ . a) Dispersion relation in lead  $\uparrow$  showing the three lowest energy modes. b) Dispersion relation in the coupling region of the split wire, showing the first 2 symmetric (full lines) and anti-symmetric (dashed lines) modes. c) Transmission probability from  $|0, \uparrow\rangle$  on the left to  $|0, \uparrow\rangle$  on the right (black full line); transmission probability from  $|1, \uparrow\rangle$  on the left to  $|1, \uparrow\rangle$  on the right (red dotted line, shifted by 1 for clarity); total transmission from the  $\uparrow$  lead on the left to the leads on the right (green dashed line). All three plots share the y-axis energy scale.

states, which eventually leads to the “dynamical modification of the interference pattern” previously calculated in ref. [15]. The physics of the current split-wire setup and the Mach-Zehnder interferometer studied in ref. [15] is very similar; the only real difference is that the two paths of the Mach-Zehnder are spatially separated while here they share the same region. Adapting the results of ref. [15] (eqs. 27 and 28 in ref. [15]) to the present case yields

$$\begin{aligned} n_{\uparrow} &= \frac{\bar{n}}{2} + \frac{1}{2\pi} \sin(\pi\bar{n}) \cos\left(\pi\bar{n} + \frac{\Delta k_0}{2} \tilde{L}\right) \\ n_{\downarrow} &= \frac{\bar{n}}{2} - \frac{1}{2\pi} \sin(\pi\bar{n}) \cos\left(\pi\bar{n} + \frac{\Delta k_0}{2} \tilde{L}\right). \end{aligned} \quad (37)$$

Figure 6b compares the results of the time-resolved simulation (symbols) with the above model (dashed lines) with  $\tilde{L}$  as a fitting parameter; we used  $\tilde{L} = 1340$ . We see a very good agreement of the numerical results with the theory.

#### IV. CONCLUSIONS

In the vast majority of devices proposed to implement qubits, one applies time-dependent excitations to a localized two level system in order to create the desired super-

position of states. In the device studied above, the philosophy is slightly different: the time-dependent potential is replaced by a spatially dependent potential and, upon sending a charge excitation inside the system, this excitation travels and *effectively* experiences a time dependent potential as it sees different regions of the sample. In a similar spirit, one could implement two-qubit gates by capacitively coupling two such devices through one arm. Such devices could be used as qubit on their own right, or perhaps more interestingly as quantum buses to couple different localized qubits.

We have performed time-resolved simulations of this split-wire flying qubit setup using cutting-edge numerical techniques. We have seen that such a system can be effectively treated as a two-path interferometer, and that applying voltage pulses to a lead of the split-wire gives rise to a modification of the d.c. interference pattern; a strictly dynamical effect. More physics needs to be included into the model to achieve realistic simulations, starting with the (self consistent) Hartree potential that leads to a renormalization of the surface plasmon velocity. However, the technology is now in place so that these types of simulation will become mature and be used as design tools for future experiments.

*Acknowledgements.* This work was supported by the ANR grant QTERA, and the ERC consolidator grant MesoQMC. We thank Christopher Bäuerle, Grégoire Roussely and Shintaro Takada for interesting discussions.

<sup>1</sup> J. Dubois, T. Jullien, F. Portier, P. Roche, A. Cavanna, Y. Jin, W. Wegscheider, P. Rouleau, and D. C. Glattli, Nature **502**, 659 (2013), ISSN 0028-0836.

<sup>2</sup> G. FÁlve, A. MahÁl, J.-M. Berroir, T. Kontos,

B. PlaĀgais, D. C. Glattli, A. Cavanna, B. Etienne, and Y. Jin, Science **316**, 1169 (2007), ISSN 0036-8075, 1095-9203.

<sup>3</sup> R. C. Ashoori, H. L. Stormer, L. N. Pfeiffer, K. W. Baldwin, and K. West, Phys. Rev. B **45**, 3894 (1992).

